# Journal of Materials Chemistry A

Accepted Manuscript

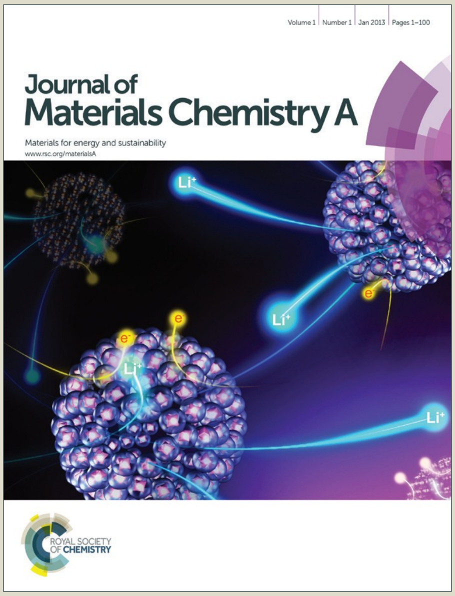

Volume 1 | Number 1 | Jan 2013 | Pages 1–100

Journal of Materials Chemistry A

Materials for energy and sustainability

www.rsc.org/materialsA

ROYAL SOCIETY OF CHEMISTRY

ROYAL SOCIETY OF CHEMISTRY

Journal of
Materials Chemistry A

Cite this: DOI: 10.1039/c0xx00000x

www.rsc.org/xxxxxx

ARTICLE TYPE

# 3-Dimensional Porous N-doped Graphene Foam as Non-Precious Catalysts for Oxygen Reduction Reaction

**Xuejun Zhou[a], Zhengyu Bai[b], Mingjie Wu[a], Jinli Qiao [a,b]*, Zhongwei Chen*[c]**

***Received (in XXX, XXX) Xth XXXXXXXXX 20XX, Accepted Xth XXXXXXXXX 20XX***
**DOI: 10.1039/b000000x**

Nitrogen-doped graphene materials have been demonstrated as the promising alternative catalysts for oxygen reduction reaction (ORR) in fuel cells and metal-air batteries due to their relatively high activity and good stability in alkaline solutions. However, they suffer from low catalytic activity in acid medium. Herein, we have developed an efficient ORR catalyst based on nitrogen doped porous graphene foams (PNGF) using hard templating approach. The obtained catalyst exhibits both remarkable ORR activity and long term stability in both alkaline and acidic solutions, and its ORR activity is even better than that of Pt-based catalyst in alkaline medium. Our results demonstrate a new strategy to rationally design highly efficient graphene-based non-precious catalysts for electrochemical energy devices.

## 1. Introduction

Oxygen reduction reaction (ORR) electrocatalysis is an extremely important research topic owing to its practical application in electrochemical energy devices such as fuel cells and metal-air batteries[1, 2]. Up until now, platinum (Pt)-based catalysts including Pt alloys have been widely used as the most efficient catalysts to catalyze the inherently sluggish ORR[3]. The high cost of Pt together with its limited natural abundance has however hindered the widespread commercial success of these electrochemical energy technologies. To overcome the cost challenges, significant efforts have focused on the development of alternative non-Pt catalysts that are based on non-precious metals and/or various heteroatom-doped carbonaceous materials[4-6]. Among the catalysts studied, nitrogen (N) doped carbon nanomaterials with high activity and good stability in alkaline medium have been explored as promising candidates[7]. The ORR catalytic activity and stability on N-doped carbons has been experimentally observed and also theoretically studied using quantum mechanical calculations, revealing that the introduction of nitrogen atoms could induce the charge delocalization of the adjacent carbon atoms, thereby facilitating oxygen adsorption and resulting in enhanced ORR activity[8-10].

Regarding the carbon-based materials, graphene, a one atom-thick, two-dimensional (2-D) monolayer carbon material, has been recognized to possess some fascinating properties such as high surface area, superior electrical conductivity, and excellent mechanical/chemical stability[11-13]. Furthermore, nitrogen doped graphene materials have also been demonstrated as efficient catalysts materials with high ORR catalytic activity in alkaline media[14-22]. However, when compared to Pt-based catalysts, these non-Pt catalysts are still less active and stable towards the ORR in acidic medium. The insufficient ORR activity and stability are probably due to the relatively low density of active site structures within these materials that are capable of catalyzing the ORR under the harsh acidic conditions. To increase the ORR active site density, a viable approach is to enlarge the volumetric surface area of the resulting graphene catalysts. However, due to the nature of 2-D materials, graphene sheets tend to irreversibly aggregate (stacking) during the fabrication process, resulting in significantly reduced surface areas. This stacking thereby causes inferior mass transport capabilities and renders a substantial number of active sites inaccessible to reactants. To address this, various methods can be applied to prevent restacking of graphene, such as covalent or noncovalent functionalization with polymers and the introduction of spacers in-between the individual layers of graphene[23, 24]. Recently, the integration of 2-D graphene sheets into 3-D porous structure, such as crumpled graphene, holey graphene or graphene foams, has also generated great interest for a wide range of applications due to their exceptional porous configuration (large surface area, and high porosity)[25-29]. For instance, Zhao *et al.*[30] successfully synthesized nanoporous graphene foams using a hard templating approach, resulting in materials with both high surface area (851 $m^2 g^{-1}$) and ultra-large pore volumes. Xu *et al.*[31] fabricated a 3-D holey graphene framework (HGF) with a hierarchical porous structure through a hydrothermal reaction and subsequent reduction process. Their HGF exhibited both high gravimetric capacitance (298 F $g^{-1}$) and high volumetric capacitance (212 F $cm^{-3}$) for a supercapacitor employing an organic electrolyte. Liu *et al.*[32] reported the synthesis of 3-D graphene foam (GF)/carbon nanotube (CNT) hybrid films by template-directed chemical vapour depostion. The as-prepared GF/CNT films deposited with $MnO_2$ and polypyrrole could be used as the electrode of flexible asymmetric supercapacitors, showing remarkable energy/power densities[32].

Through all these investigations, it has been widely recognized that porous graphene materials have large surface areas and diversified porosity for both enhanced electrolyte–electrode interactions and electrolyte–reactant diffusion. Therefore, it is expected that 3-D porous graphene-based materials have great application potential as high performance catalyst designs for fuel cell technologies. Herein, we develop an efficient ORR catalyst based on nitrogen doped porous graphene foams prepared using a hard templating approach. The obtained catalyst exhibits promising ORR activity and stability in acidic solutions, along with performance in alkaline that surpasses state-of-the-art commercial Pt/C catalyst. The outstanding electrochemical performance thereby makes it a very promising non-precious metal catalyst substitute to commercial Pt/C in fuel cell systems.

## 2. Experimental section

### 2.1 Preparation of graphene oxide suspension

Graphite oxide was synthesized using a modified Hummers method[33]. Briefly, graphite (3 g) was dispersed in a concentrated acid mixture of $H_2SO_4$ and $H_3PO_4$. After the addition of $KMnO_4$ (9 g), the solution was heated at 50 °C for 12 hours, after which it was poured onto ice (400 mL), followed by the addition of $H_2O_2$ (10 mL). After washing with HCl solution and deionized water, the as-prepared graphite oxide was dispersed in ethanol, and sonicated for 2 hours to form a homogeneous graphene oxide suspension (~5.0 mg $mL^{-1}$).

### 2.2 Synthesis of porous nitrogen-doped graphene foam (PNGF)

The PNGF was synthesized using silica spheres as the hard template. Typically, 1.0 g silica spheres (particle size ~7 nm) were first dispersed in 20 mL ethanol. The suspension was continuously stirred while 200 mg $FeCl_2$ $4H_2O$ and 700 mg dicyandiamide were added. After complete dissolution, the graphene oxide suspension (30 mL) was added into the solution. They were mixed together by stirring for 24 hours at 60 °C and then dried at 85 °C in an oven overnight. The dried precipitate was pyrolyzed at 900 °C for 1 hour under nitrogen atmosphere. The obtained composites were then immersed into a solution consisting of HF (5%) and HCl (10%) with stirring for 24 hours to simultaneously remove silica particles and inactive metal species. Finally, the catalyst sample was heat-treated again in nitrogen atmosphere at 900 °C for 1 hour. For comparison, NG and PNG were also synthesized by the procedure mentioned above, except that silica and transition metal were not added, respectively.

### 2.3 Sample characterizations

Transmission electron microscopy (TEM) analyses were performed on a high-resolution Hitachi JEM-2100 system operating at 200 kV. The Brunauer–Emmett–Teller (BET) method was used to determine the specific surface area by measuring the adsorption of $N_2$ using an ASAP2020 volumetric adsorption analyzer (Micromeritics, U.S.A.). The specific surface area was determined by standard BET method in a relative pressure range of 0.05 – 0.3. The pore size distribution curves were calculated by the nonlocal density functional theory. Raman spectra were collected on a Via-Reflex microscopic confocal Raman spectrometer with a 633 nm laser excitation. Surface analysis of the catalyst particles was carried out by XPS on an RBD-upgraded PHI-5000C ECSA system (PerkinElmer) with an Al K X-ray anode source (hν =1486.6 eV) at 14.0 kV and 250 W.

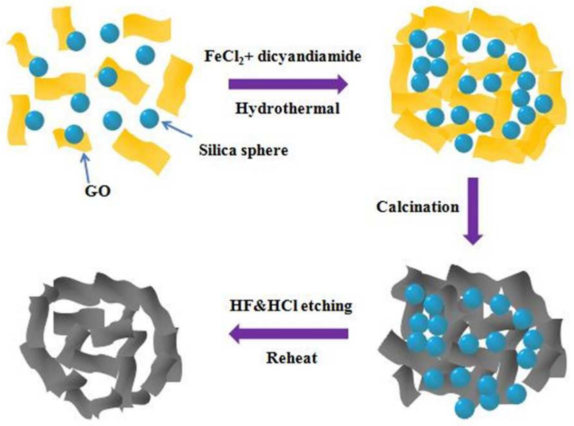

**Scheme 1** Schematic illustration of the synthesis procedures of the porous nitrogen-doped graphene foam (PNGF).

### 2.4 Electrochemical measurements

Electrochemical measurements were performed using a CHI Electrochemical Station (760D) in a standard three-electrode cell. The counter electrode and reference electrode were a graphite rod and a saturated calomel electrode, respectively. All reported potentials were converted to the RHE scale. The catalyst ink was prepared by ultrasonically blending 4 mg of catalyst and 8 $\mu$l of 5 wt% Nafion® in 1 ml of solution containing water and ethanol, 4:1 by volume for more than 1 hour. Before RDE and RRDE measurements, 30 $\mu$l of ink solution was applied to the disk, resulting in a catalyst loading of 0.485 mg $cm^{-2}$. The reference Pt/C catalyst ink was prepared by ultrasonically blending 4 mg of 20 wt% Pt/C (JM) and 8 $\mu$l of 5 wt% Nafion® in 1 ml of ethanol for more than 1 hour. For the Pt/C reference catalyst, a platinum wire was used as the counter electrode. All electrochemical tests were performed at a room temperature in oxygen-saturated 0.1 M KOH or 0.1 M $HClO_4$. Before each measurement, the electrolyte was bubbled with $O_2$ for 30 minutes. A flow of $O_2$ was maintained over the electrolyte during the measurement to ensure a continuous $O_2$ saturation. Linear sweep voltammetry was conducted at the same conditions in $N_2$-saturated electrolyte to substract the background capacative current. The onset potential was defined as the potential at which the background subtracted current density was equal to -0.1 mA $cm^{-2}$ [34].

## 3. Results and Discussion

A schematic illustration of the synthetic procedure for the porous nitrogen-doped graphene foam (PNGF) is depicted in Scheme 1. It can be seen that the PNGF is prepared via the strategic combination of nitrogen precursors, transition metal salts, graphene oxide (GO), and spherical silica templates. In the first step, silica spheres were dispersed in ethanol by sonication. After adding dicyanamide, ferrous chloride and graphene oxide, the mixture is hydrothermally treated. The as-prepared composite is then pyrolyzed under an inert atmosphere to further reduce GO and introduce nitrogen atoms into the graphene. Finally, the porous graphene foam is obtained by etching the silica templates and soluble surface iron species, followed by a second pyrolysis in an inert atmosphere.

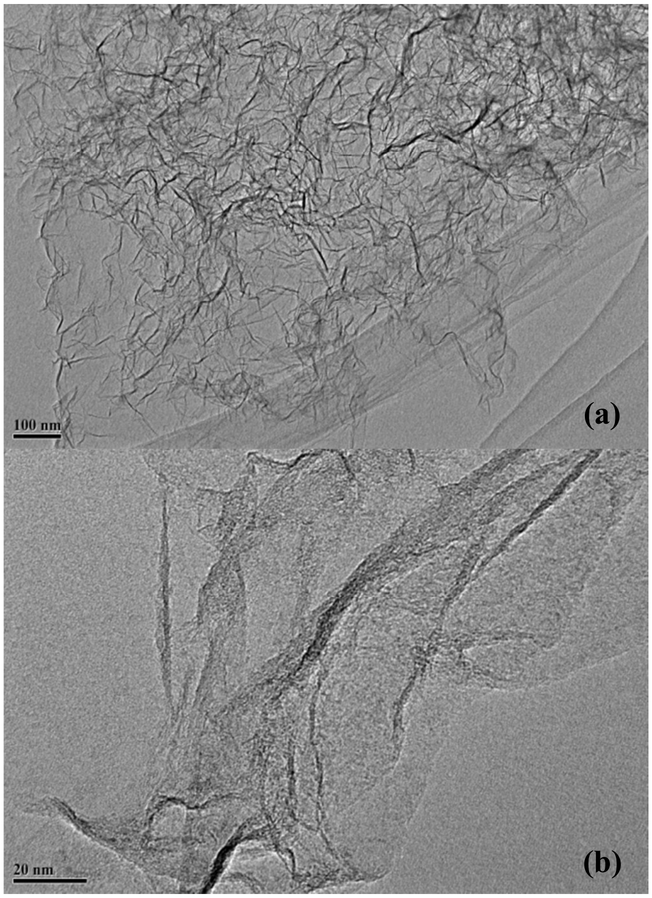

**Figure 1.** Typical TEM images of PNGF with two different magnifications.

The morphology and microstructure of the PNGF were first characterized by transmission electron microscopy (TEM). As displayed in Figure 1(a), PNGF shows a crumpled silk veil like morphology which is similar to that of porous graphene foam. This crumpled morphology is also commonly observed on the reduced graphene oxide, which is partially induced by the defective structures formed upon exfoliation of graphite or the presence of doped heteroatoms[35]. It can also be seen that highly interconnected crumpled and scrolled graphene sheets closely associate with each other to form a 3-D structure, which can effectively prevent the aggregation of 2-D graphene sheets. The higher resolution HRTEM image shown in Figure 1(b) further confirms that the three-dimensional porous foam-like structure is constructed by graphene sheets.

Nitrogen isothermal adsorption/desorption measurements were performed to investigate the porous features of the catalysts. The $N_2$ adsorption-desorption plots of PNGF, as shown in Figure 2(a), exhibit a type-IV isotherm with a steep increase of nitrogen absorption at a relative high pressure, indicating the existence of mesopores. Furthermore, the rapid rise in the low pressure region also indicates the presence of micropores. Using these plots, it was calculated that PNGF had a high BET surface area of 670 $m^2$ $g^{-1}$. The pore size distribution plots (Figure 2(a) insert) exhibits a feature of multi-peaks in the range of 0 - 60 nm, confirming the hierarchical porous structure in the catalyst. It is worth noting that the pores in the catalyst did not directly replicate the sizes and shape of the used silica template, but much enlarged meso- and macropores were obtained. Unlike the functional porous graphene foam with size-defined mesopores[30], the PNGF prepared by this method has a more complicated hierarchical structure. This may be explained by the phase separation during the fabrication process[30]. As is well documented, the hierarchical porous architecture is ideal for ORR due to the fact that active sites are predominately formed in the smaller micropores, while the larger pores can serve as reactive molecules reservoirs and thus shorten the diffusion pathways of reactive molecules to and from the micropores[36, 37]. Hence, it is expected that PNGF should be able to deliver superior electrochemical performance for ORR. For comparison, the nitrogen-doped graphene (NG) catalyst, which was prepared without using a silica template, displayed a BET surface area of only 384 $m^2$ $g^{-1}$ (Figure S1(a)). This value is

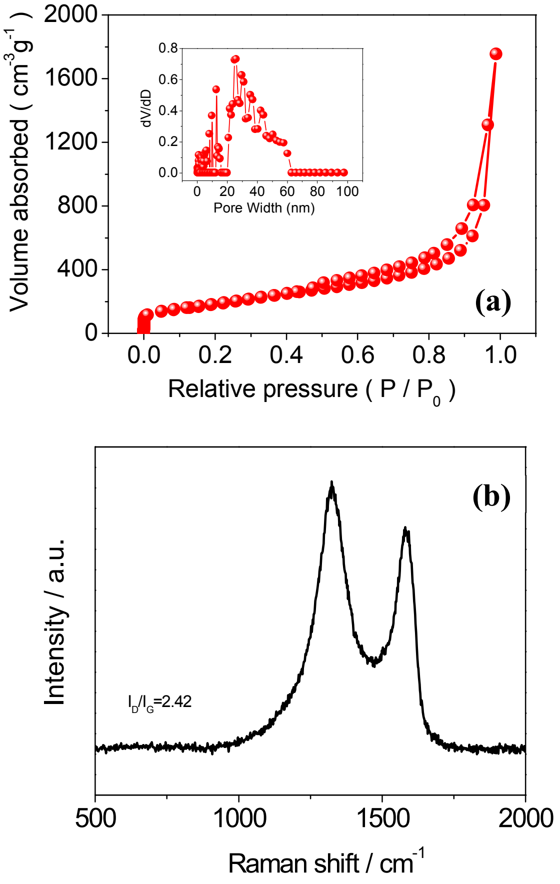

**Figure 2**. (a) $N_2$ adsorption/desorption isotherms of PNGF, the insert is the pore size distribution; and (b) Raman spectra of PNGF.

comparable to that of the reported functional graphene nanomesh foam (362 $m^2$ $g^{-1}$)[38]. In our work, the BET specific surface area could be increased dramatically from 384 $m^2$ $g^{-1}$ for NG to 670 $m^2$ $g^{-1}$ for PNGF after the addition of spherial silica (Figure S1(b)). These results demonstrate that the introduction of silica during the fabrication process can effectively decrease the aggregation of graphene sheets and thus increase the surface area.

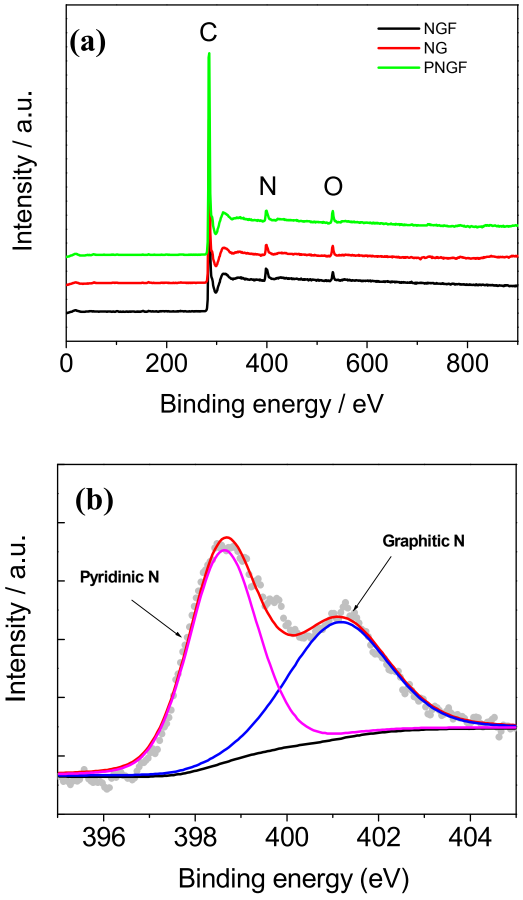

**Figure 3**. (a) XPS survey spectra of NG, NGF, and PNGF, respectively; and (b) High resolution N1s XPS spectra of PNGF.

Raman spectroscopy was used to provide information on the degree of the structural defects. Figure 2(b) shows the Raman spectra of PNGF. Two prominent peaks are observed, corresponding to the characteristic D (1324 $cm^{-1}$) and G (1580 $cm^{-1}$) bands for graphitic carbon. The D band is a common feature of all disordered graphitic carbon, while the G band is closely related to the $sp^2$-hybridized carbon atoms residing in the hexagonal framework structure. In particular, the ratio of the D band to G band intensity ( $I_D/I_G$) is considered a key parameter to evaluate the degree of structural defects in graphitic materials, whereby a higher ratio suggests an increased concentration of defects. Interestingly, PNGF exhibits a strong D-band signal and a lower intensity G band with a $I_D/I_G$ of 2.42. This value is larger than that of GO (1.93) (Figure S2), implying that PNGF possesses a much higher disordered graphitic structures. This can be ascribed to the highly crumpled structure and the introduction of defects by nitrogen-doping. The ratio of $I_D/I_G$ for NG is 2.45, comparable to the value of PNGF. The highest $I_D/I_G$ ratio (2.86) of PNG among the three samples reflects the presence of more defective sites. The above results indicate that Fe may be an important factor affected the degree of graphitization.

X-ray photoelectron spectroscopy (XPS) was also conducted to elucidate the chemical structure of the resulting PNGF and the results have been summarized in Table S1. As shown in Figure 3, only C1s, N1s, and O1s signals can be observed for all samples in the XPS spectra. There are no silica or metallic species detected in the survey spectrum of PNGF, suggesting that these species on the surface of PNGF can be successfully removed by washing with hydrofluoric acid and hydrochloric acid solutions. The presence of nitrogen suggests efficient N-doping in the graphene network. The nitrogen content in the PNGF is about 5.07 at%, which is comparable to results achieved previously when using $NH_3$ to facilitate nitrogen-doping method[35, 39]. The complex N1s spectra can generally be further deconvoluted into two primary peaks (as shown in Figure 3(b), Figure S3), which correspond to pyridinic N (398.6 ± 0.3 eV) and graphitic N (401.3 ± 0.3 eV), respectively[40]. Pyridinic N refers to N atoms at the edges or defects of the graphene planes, where each N atom bonds with two carbon atoms and contributes one $p$-electron to the aromatic $\pi$ system. Graphitic N is within a graphite plane and bonded to three carbon atoms. These two species are believed to play roles in the ORR process[41, 42].

To demonstrate the efficient electrochemical activity of PNGF for the ORR, cyclic voltammograms were first obtained in $O_2$- and $N_2$-saturated 0.1 M KOH aqueous solution at a scan rate of 50 mV $s^{-1}$. As shown in Figure 4(a), a featureless voltammetric curve can be observed under $N_2$ saturation in the potential range of 0.2 V to 1.1 V, which is ascribed to the typical double-layer capacitive current of porous carbon materials. In contrast, when oxygen is introduced, a profound cathodic current with an onset potential of 1.02 V vs. RHE is clearly observed, demonstrating that the PNGF has very high catalytic activity towards the ORR.

To further evaluate the electrocatalytic activity of PNGF, rotating disk electrode (RDE) measurements were also employed. Figure 4(b) shows the polarization curves for different samples. For the purpose of comparison, a linear sweep voltammogram (LSV) of commercial 20 wt% Pt/C was also obtained. From Figure 4(b), it can be clearly seen that the lowest ORR activity (in terms of onset potential) is the sample prepared without transition metal (PNG). After introducing a transition metal, the ORR onset potential shifts positively about 65 mV for NG and PNGF, approaching that of commercial Pt/C (1.03 V). However, due to insufficient $O_2$ transfer in the catalyst layer, the NG still shows much less catalytic activity. Notably, a further enhancement is observed with simultaneous addition of the silica nanoparticles and transition metal for PNGF, under which a half-wave potential of 0.86 V is achieved. In a relatively high potential region, a nearly identical ORR polarization curve to that of Pt/C can be seen. At potentials lower than 0.88 V versus RHE, the ORR current density catalyzed by PNGF is even greater than that of Pt/C. It should be noted here that the Pt/C catalyst shows a half wave potential of 0.877 V, which is comparable to the performance of the state-of-the-art Pt/C previously reported in the literature[39]. The mass transport-limiting current of PNGF in the

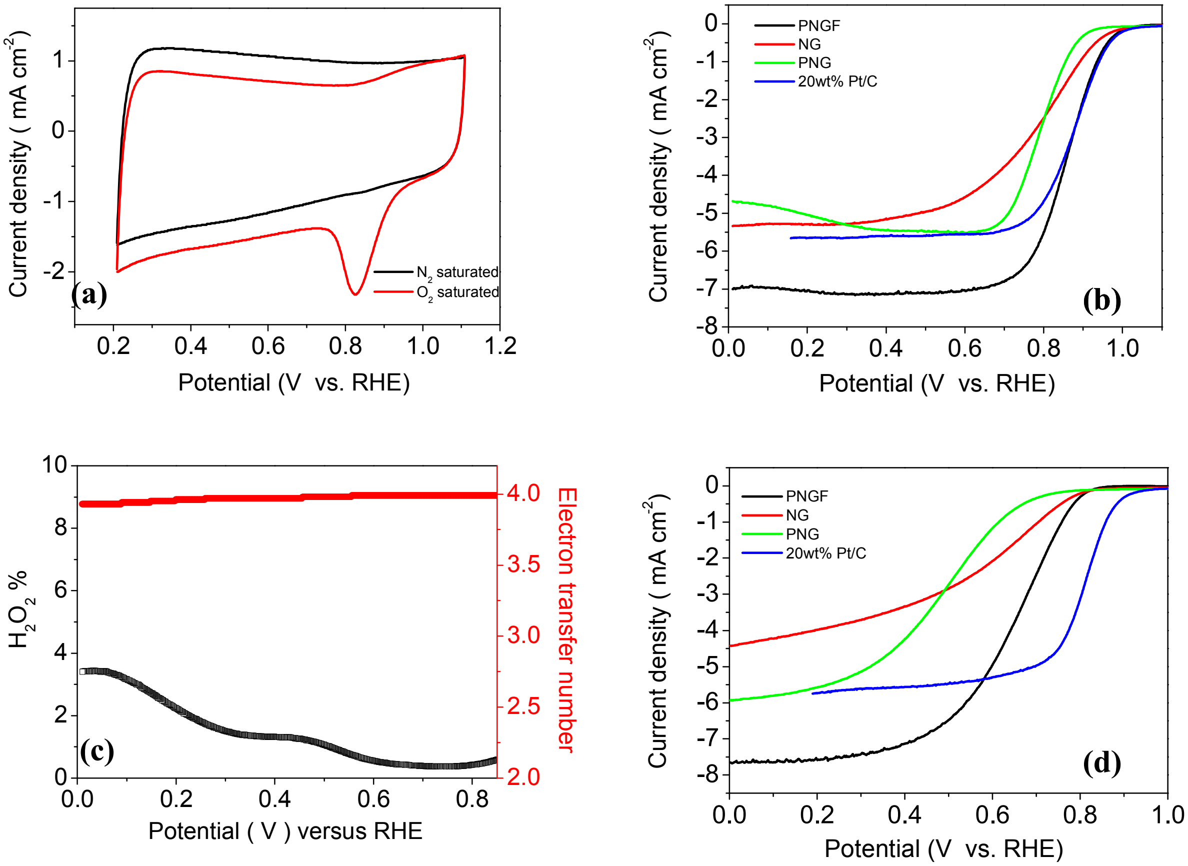

**Figure 4.** (a) Cyclic voltammograms of PNGF in in $N_2$- and $O_2$ -saturated 0.1 M KOH at a scan rate of 50 mV s$^{-1}$; (b) Linear sweep voltammograms of various electrocatalysts on a rotating disk electrode (1600 rpm) in $O_2$-saturated 0.1 M KOH at a scan rate of 5 mV s$^{-1}$; (c) Percentage of $H_2O_2$ produced and electron transfer number of PNGF (1600rpm) , and (d) Linear sweep voltammograms of various electrocatalysts on a rotating disk electrode (1600 rpm) in $O_2$-saturated 0.1 M $HClO_4$ at a scan rate of 5 mV s$^{-1}$.

polarization curve approaches ~7 mA cm$^{-2}$. To the best of our knowledge, this is the highest value in the reported porous graphene materials. Obviously, the improved performance may be attributed to both the increased surface area and high density of active sites, indicating that the hierarchical porous structure in the PNGF has a positive effect on the ORR activity.

To investigate the ORR catalytic pathway of the catalyst, rotating ring–disk electrode (RRDE) measurements were also performed to monitor the peroxide yield on the PNGF catalyzed electrode. As shown in Figure 4(c), the peroxide yield on the PNGF electrode is found to be less than 4% over the potential range of from 0 V to 0.85 V. The corresponding electron transfer number is higher than 3.9, suggesting the complete reduction of oxygen into water.

Next, the electrocatalytic performance of the catalysts in acidic medium was also investigated. As shown in Figure 4(d), the electrochemical activities in acid follow the same trend with those observed in alkaline media. The catalysts with metal exhibit higher ORR onset potential than the metal free catalyst. Still, the catalyst without silica has inferior mass-transport of reactive molecules in the catalyst layer. The PNGF catalyst shows the highest ORR catalytic activity in acidic media, with an onset potential of 0.83 V vs. RHE and well-defined mass transport-limited current density in the RDE polarization curve. Moreover, PNGF also exhibits an ORR process that occurs mainly through a 4-electron transfer pathway with a low $H_2O_2$ yield of 6.72-9.36% over the entire potential range measured (Figure S5a).

To gain deeper insight into the mechanism of ORR, it is necessary to identify the role of iron in forming the active sites in the catalyst. Previous studies have revealed that introducing transition metals into the nitrogen containing complex could further enhance the ORR catalytic activity[43]. However, the exact role of transition metals has not been well understood. Some studies argued that metal could only help the formation of active sites, while the others believe that the metal could be an integral acitve part of the catalytic site. Usually, studies of active sites were mainly based on ex-situ spectroscopic techniques, such as XPS, Mössbauer spectroscopy, and X-ray absorption spectroscopy,[44-46] as well as electrochemical tests [47-49]. In general, most electrochemical poisoning tests for studying the role of metal in the catalysts are conducted in alkaline media, and there are few electrochemical experiments performed in acidic medium, mainly due to the absence of proper ORR probes[50]. Recently, Sun *et al.*[51] found that the ORR activity in acidic media could be suppressed significantly by low valence state sulfur-containing species, thus confirmed that the active sites contained Fe element

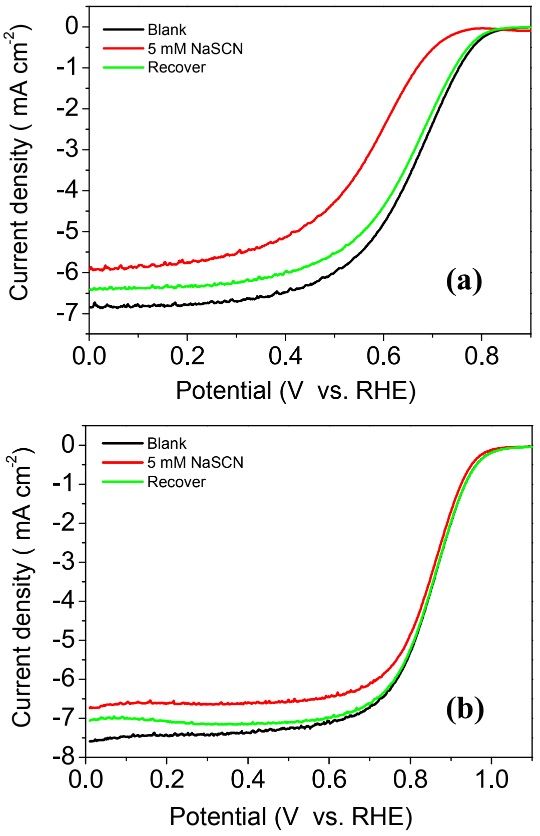

**Figure 5.** (a) Linear sweep voltammograms of PNGF on a rotating disk electrode (1600 rpm) in $O_2$-saturated 0.1 M $HClO_4$ (with and without NaSCN) at a scan rate of 5 mV s$^{-1}$; (b) Linear sweep voltammograms of PNGF on a rotating disk electrode (1600 rpm) in $O_2$-saturated 0.1 M KOH (with and without NaSCN) at a scan rate of 5 mV s$^{-1}$.

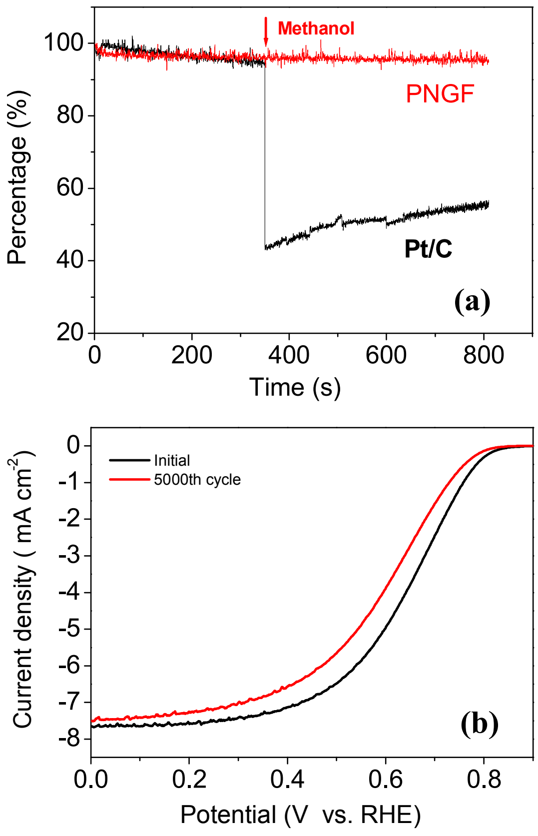

**Figure 6.** (a) Chronoamperometric responses of PNGF, Pt/C at 0.6 V in 0.1 M KOH followed by addition of 3M methanol; (b) Linear sweep voltammograms of PNGF on a rotating disk electrode (1600 rpm) before and after 5000 cycles in $O_2$-saturated 0.1 M $HClO_4$ at a scan rate of 5 mV s$^{-1}$.

in acidic medium[51]. In our study, we employed $SCN^-$ as a probe in both acidic and alkaline medium. Although there is no metal species being detected in the XPS spectra, it does not mean there is no metal reside in the catalyst due to the limited analytic sensitivity of XPS. In our work, inductively coupled plasma atomic emission spectrometry (ICP-AES) revealed an iron content of 1.83 wt%, confirming the presence of trace metals after the acid wash. This value is close to the residual metal in the carbon nanotube–graphene complexes[39]. According to the reported literatures, even an extremely small amount of metallic impurities in the catalysts might have a strong influence on the ORR[52,53]. As shown in Figure 5(a), the ORR activity is significantly inhibited by the introduction of NaSCN in the acidic media, suggesting that the Fe ion is the active centre in the catalyst. After washing the catalyst to remove $SCN^-$ ions absorbed on the active sites, the ORR activity is almost fully recovered, further confirming that Fe ion is the active centre in the catalyst. Interestingly, PNGF shows less activity loss in the presence of $SCN^-$ in alkaline medium (Figure 5(b)). These results likely suggest a different catalytic mechanism and active site structures between acidic and alkaline media[54, 55].

For potential use in direct methanol fuel cells, the methanol poisoning effects should also be considered. We therefore measured chronoamperometric curve to examine the possible selectivity effect. As expected, in the cases of PNGF, no noticeable response can be observed after the addition of methanol in alkaline medium (Figure 6(a)). In contrast, a drastic decrease in the ORR activity of Pt/C is detected once methanol is added under the same testing conditions. To our interest, the PNGF catalyst showed no any activity loss for ORR even in acidic solution in the presence of methanol (Figure S7). These results indicate that beyond the excellent electrocatalytic activity, the PNGF catalyst also exhibits a high selectivity for ORR with excellent tolerance to methanol poisoning effects. The durability is another important key parameter of fuel cell catalysts that needs to be considered. In this regard, the durability of the catalyst was assessed by a cycling durability test in $O_2$-saturated acidic solution in the potential range of 0.6–1.0 V at a scan rate of 50 mV s$^{-1}$, as suggested by the US Department of Energy's accelerated durability test protocol. After 5,000 continuous cycles, the half-wave potential $E_{1/2}$ exhibited a small negative shift of about 39 mV under $O_2$ cycling (Figure 6(b)). The stability of the PNGF is comparable to that of the previously reported metal-free ORR catalysts[16]. In addition, the PNGF catalyst showed high stability in alkaline solutions, with a small shift of only about 15 mV after 5,000 cycles (Figure S8).

## 4. Conclusion

In summary, we have successfully synthesized an efficient ORR catalyst based on nitrogen doped porous graphene foams using a hard templating approach. With 3-D macroporous morphology and a high surface area, the obtained catalyst demonstrates a perfect ORR activity, excellent tolerence to methanol and high stability in both acidic and alkaline solutions. The outstanding electrochemical performance makes it a very promising candidate for practical applications as a non-precious metal catalyst in metal-air batteries and fuel cells.

## Acknowledgements

This work was supported by the National Natural Science Foundation of China (21173039); Specialized Research Fund for the Doctoral Program of Higher Education, SRFD (20110075110001) of China; International Academic Cooperation and Exchange Program of Shanghai Science and Technology Committee (14520721900), the Fundamental Research Funds for the Central Universities, and College of Environmental Science and Engineering, State Environmental Protection Engineering Center for Pollution Treatment and Control in Textile Industry, Donghua University, Shanghai 201620, China. All the financial supports are gratefully acknowledged.

## Notes and references

[a] *College of Environmental Science and Engineering, Donghua University, 2999 Ren'min North Road, Shanghai 201620, P. R. China. Fax: +86-21-67792159; Tel: +86-21-67792379; E-mail: qiaojl@dhu.edu.cn*

[b] *Department of Chemical Engineering, E6-2006, University of Waterloo, 200 University Avenue West, Waterloo, ON, N2L 3G1, Canada; Tel: 1-226-338-3238; E-mail: zhwchen@uwaterloo.ca*

*†Electronic Supplementary Information (ESI) available: [details of any supplementary information available should be included here]. See DOI: 10.1039/b000000x/*

1 S. Guo, S. Zhang and S. Sun, *Angew. Chem. Int. Ed.*, 2013, **52**, 8526-8544.
2 Y. J. Wang, D. P. Wilkinson and J. Zhang, *Chem. Rev.*, 2011, **111**, 7625-7651.
3 A. Chen and P. Holt-Hindle, *Chem. Rev.*, 2010, **110**, 3767-3804.
4 F. Jaouen, E. Proietti, M. Lefevre, R. Chenitz, J.-P. Dodelet, G. Wu, H. T. Chung, C. M. Johnston and P. Zelenay, *Energy Environ. Sci.*, 2011, **4**, 114-130.
5 Z. Chen, D. Higgins, A. Yu, L. Zhang and J. Zhang, *Energy Environ. Sci.*, 2011, **4**, 3167-3192.
6 Q. Li, R. Cao, J. Cho and G. Wu, *Adv. Energy. Mater.*, 2014, **4**,1301415.
7 D.-W. Wang and D. Su, *Energy Environ. Sci.*, 2014, **7**, 576-591.
8 K. Gong, F. Du, Z. Xia, M. Durstock and L. Dai, *Science*, 2009, **323**, 760-764.
9 L. Qu, Y. Liu, J.-B. Baek and L. Dai, *ACS Nano*, 2010, **4**, 1321-1326.
10 S. Wang, D. Yu, L. Dai, D. W. Chang and J.-B. Baek, *ACS Nano*, 2011, **5**, 6202-6209.
11 A. Ambrosi, C. K. Chua, A. Bonanni and M. Pumera, *Chem. Rev.*, 2014, **114**, 7150-7188.
12 H.-P. Cong, J.-F. Chen and S.-H. Yu, *Chem. Soc. Rev.*, 2014, **43**, 7295-7325.
13 B. Xia, Y. Yan, X. Wang and X. W. Lou, *Mater. Horizons*, 2014, **1**, 379-399.
14 H. Wang, T. Maiyalagan and X. Wang, *ACS Catal.*, 2012, **2**, 781-794.
15 M. Liu, R. Zhang and W. Chen, *Chem. Rev.*, 2014, **114**, 5117-5160.
16 W. Wei, H. Liang, K. Parvez, X. Zhuang, X. Feng and K. Mullen, *Angew. Chem. Int. Ed.*, 2014, **53**, 1570-1574.
17 J. Liang, Y. Jiao, M. Jaroniec and S. Z. Qiao, *Angew. Chem. Int. Ed.*, 2012, **51**, 11496-11500.
18 Y. Zheng, Y. Jiao, L. Ge, M. Jaroniec and S. Z. Qiao, *Angew. Chem. Int. Ed.*, 2013, **52**, 3110-3116.
19 Z. Yang, H. Nie, X. a. Chen, X. Chen and S. Huang, *J. Power Sources*, 2013, **236**, 238-249.
20 D. Geng, N. Ding, T. S. Andy Hor, Z. Liu, X. Sun and Y. Zong, *J. Mater. Chem. A*, 2015, DOI: 10.1039/C4TA06008C.
21 H. Yin, C. Zhang, F. Liu and Y. Hou, *Adv. Funct. Mater.*, 2014, **24**, 2930-2937.
22 J. Liang, X. Du, C. Gibson, X. W. Du and S. Z. Qiao, *Adv. Mater.*, 2013, **25**, 6226-6231.
23 X. Zhou, J. Qiao, L. Yang and J. Zhang, *Adv. Energy Mater.*, 2014, **4**, 1301523.
24 H. Bai, C. Li and G. Shi, *Adv. Mater.*, 2011, **23**, 1089-1115.
25 V. Chabot, D. Higgins, A. Yu, X. Xiao, Z. Chen and J. Zhang, *Energy Environ. Sci.*, 2014, **7**, 1564-1596.
26 S. Han, D. Wu, S. Li, F. Zhang and X. Feng, *Adv. Mater.*, 2014, **26**, 849-864.
27 L. Jiang and Z. Fan, *Nanoscale*, 2014, **6**, 1922-1945.
28 C. Li and G. Shi, *Nanoscale*, 2012, **4**, 5549-5563.
29 C. Li and G. Shi, *Adv. Mater.*, 2014, **26**, 3992-4012.
30 X. Huang, K. Qian, J. Yang, J. Zhang, L. Li, C. Yu and D. Zhao, *Adv. Mater.*, 2012, **24**, 4419-4423.
31 Y. Xu, Z. Lin, X. Zhong, X. Huang, N. O. Weiss, Y. Huang and X. Duan, *Nat. Commun.*, 2014, **5**, 4554.
32 J. Liu, L. Zhang, H. B. Wu, J. Lin, Z. Shen and X. W. Lou, *Energy Environ. Sci.*, 2014, DOI: 10.1039/C4EE01475H.
33 D. C. Marcano, D. V. Kosynkin, J. M. Berlin, A. Sinitskii, Z. Sun, A. Slesarev, L. B. Alemany, W. Lu and J. M. Tour, *ACS nano*, 2010, **4**, 4806-4814.
34 D. Singh, J. Tian, K. Mamtani, J. King, J. T. Miller and U. S. Ozkan, *J. Catal.*, 2014, **317**, 30-43.
35 S. Yang, L. Zhi, K. Tang, X. Feng, J. Maier and K. Müllen, *Adv. Funct. Mater.*, 2012, **22**, 3634-3640.
36 F. Jaouen, M. Lefèvre, J.-P. Dodelet and M. Cai, *J. Phys. Chem. B*, 2006, **110**, 5553-5558.
37 H. W. Liang, X. Zhuang, S. Bruller, X. Feng and K. Mullen, *Nat. Commun.*, 2014, **5**, 4973.
38 Y. Zhao, C. Hu, L. Song, L. Wang, G. Shi, L. Dai and L. Qu, *Energy Environ. Sci.*, 2014, **7**, 1913-1918.
39 Y. Li, W. Zhou, H. Wang, L. Xie, Y. Liang, F. Wei, J.-C. Idrobo, S. J. Pennycook and H. Dai, *Nat. Nanotechnol.*, 2012, **7**, 394-400.
40 G. Wu, N. H. Mack, W. Gao, S. Ma, R. Zhong, J. Han, J. K. Baldwin and P. Zelenay, *ACS nano*, 2012, **6**, 9764-9776.
41 L. Lai, J. R. Potts, D. Zhan, L. Wang, C. K. Poh, C. Tang, H. Gong, Z. Shen, J. Lin and R. S. Ruoff, *Energy Environ. Sci.*, 2012, **5**, 7936-7942.
42 C. Zhang, R. Hao, H. Liao and Y. Hou, *Nano Energy*, 2013, **2**, 88-97.
43 K. Parvez, S. Yang, Y. Hernandez, A. Winter, A. Turchanin, X. Feng and K. Müllen, *ACS Nano*, 2012, **6**, 9541-9550.
44 U. I. Kramm, M. Lefevre, N. Larouche, D. Schmeisser and J. P. Dodelet, *J. Am. Chem. Soc.*, 2014, **136**, 978-985.
45 J. Tian, A. Morozan, M. T. Sougrati, M. Lefevre, R. Chenitz, J. P. Dodelet, D. Jones and F. Jaouen, *Angew. Chem. Int. Ed.*, 2013, **52**, 6867-6870.
46 T. Xing, Y. Zheng, L. H. Li, B. C. C. Cowie, D. Gunzelmann, S. Z. Qiao, S. Huang and Y. Chen, *ACS Nano*, 2014, **8**, 6856-6862.
47 W. Li, J. Wu, D. C. Higgins, J.-Y. Choi and Z. Chen, *ACS Catal.*, 2012, **2**, 2761-2768.
48 M. S. Thorum, J. M. Hankett and A. A. Gewirth, *J. Phys. Chem. Lett.*, 2011, **2**, 295-298.
49 C. H. Choi, H.-K. Lim, M. W. Chung, J. C. Park, H. Shin, H. Kim and S. I. Woo, *J. Am. Chem. Soc.*, 2014, **136**, 9070-9077.
50 D. Singh, K. Mamtani, C. R. Bruening, J. T. Miller and U. S. Ozkan, *ACS Catal.*, 2014, **4**, 3454-3462.
51 Q. Wang, Z.-Y. Zhou, Y.-J. Lai, Y. You, J.-G. Liu, X.-L. Wu, E. Terefe, C. Chen, L. Song and M. Rauf, *J. Am. Chem. Soc.*, 2014, **136**, 10882-10885.

52 L. Wang, A. Ambrosi and M. Pumera, *Angew. Chem. Int. Ed.*, 2013, **52**, 13818-13821.

53 J. Liu, X. Sun, P. Song, Y. Zhang, W. Xing and W. Xu, *Adv. Mater.*, 2013, **25**, 6879-6883.

54 U. Tylus, Q. Jia, K. Strickland, N. Ramaswamy, A. Serov, P. Atanassov and S. Mukerjee, *J. Phys. Chem. C*, 2014, **118**, 8999-9008.

55 N. Ramaswamy, U. Tylus, Q. Jia and S. Mukerjee, *J. Am. Chem. Soc.*, 2013, **135**, 15443-15449.